PORE-SCALE SIMULATION OF LIQUID METAL INFILTRATION INTO CERAMIC FOAM FILTERS

[1]Eric WERZNER, [2]Emiel SPEETS, [1]Hartmut KRAUSE, [1]Subhashis RAY

[1]TU Bergakademie Freiberg, Institute of Thermal Engineering, Chair of Gas and Heat Technology, Freiberg, Germany, EU, ray@iwtt.tu-freiberg.de

[2]Foseco Nederland BV, Enschede, Netherlands, EU, emiel.speets@vesuvius.com

https://doi.org/10.37904/metal.2026.5234

Abstract

During the production of metal cast parts for safety-critical applications, it is common practice to reduce unwanted impurities by filtration of the liquid metal using ceramic foam filters before the melt enters the casting mold. A critical stage of the filtration process is the infiltration of the ceramic foam during start-up (commonly called priming), especially when the filter cannot be preheated, as heat loss to the filter may lead to freezing and possibly casting failure, usually requiring foundries to use higher casting temperatures. The present study is motivated by reducing this risk through an improved understanding of its sensitivity with respect to the process parameters and geometric properties of the filter. Therefore, the infiltration process was numerically simulated using a 2D pore-scale model, enabling extensive parameter variations. The results are consistent with experimental observations of the process, provide insights into the detailed mechanisms promoting freezing, and offer guidance for improved process control and filter geometry design.

Keywords: Ceramic foam filter, priming, infiltration, CFD, pore-scale simulation

1. INTRODUCTION

Metal melt filtration is a widely established procedure in the industrial production of cast metal components. By removing unwanted impurities from the molten metal and reducing turbulence in the melt stream, the quality of the final product is significantly improved, e.g. by enhancing strength, toughness and corrosion resistance. Among the various filtration technologies, ceramic foam filters (CFF) are the most commonly employed. These open-cell foams exhibit porosities of approx. 80% and typical pore sizes on the order of a few millimeters. Their intricate network of thin struts intercepts inclusions effectively but also provides a low flow resistance and sufficient mechanical strength to withstand the hydrodynamic and thermomechanical stresses exerted by the hot melt flow. [1]

The efficiency of filtration, defined as the fraction of inclusions removed from the melt, depends on numerous parameters, including melt and inclusion properties, process conditions, and characteristics of the filter geometry. In particular, the geometric characteristics strongly influence filtration performance. Parameters such as pore density (commonly specified in pores per inch, PPI), open porosity, the cross-sectional and axial shape of the struts, and their alignment relative to the flow direction have all been shown to affect inclusion removal. Insights into these relationships can inform the design of optimized filter geometries, which are increasingly feasible to manufacture at industrial scale using 3D printing. [2]

While previous research efforts focused on improving filter performance under continuous filtration conditions, the priming stage, during which the melt infiltrates the filter, has received comparatively less attention. During this stage, a higher flow resistance occurs as a consequence of: 1) the increase in interfacial energy and 2) the heat loss to the filter, which can cause viscosity increase or freezing. Hence, the requirements during this phase differ substantially from those of high filtration efficiency during the continuous stage. For example,

although higher pore density improves filtration efficiency, it also increases the risk of freezing during infiltration due to enhanced heat transfer. Mitigating this risk by increasing the superheat temperature of the melt comes at the cost of higher energy demand, while increasing the preheat temperature of the filter may not be possible, e.g. in case of carbon-bonded filters in presence of air and for safety reasons.

It is evident that the development of filter geometries with excellent properties during all process stages requires a good understanding of the infiltration process and its sensitivity to both filter geometry and process parameters. To this end, a two-dimensional numerical model of the infiltration process was developed and employed in an extensive parametric study. This paper is structured as follows: in the next section, the numerical model is presented. Subsequently, the results as well as the conclusions will be provided.

2. NUMERICAL MODELING

In order to investigate the non-isothermal infiltration process, a detailed pore-scale numerical model was set up, which shall be presented in the following.

2.1 Physics modeling

The employed solver is based on the OpenFOAM application icoReactingMultiphaseInterFoam, which is an extension to the interFoam solver [3]. It solves the incompressible Navier-Stokes equations and the energy equation in the entire domain, including the solid struts of the filter. Multiple phases are handled through the volume-of-fluid (VOF) approach, where an individual transport equation is solved for each of the four phases (liquid metal, solid metal, filter, gas). In mushy and solid regions, the flow is dampened by a Darcy-type resistance term in the momentum equation, as typical for the enthalpy-porosity formulation [4]. The effect of surface tension is captured using the well-known continuum surface force (CSF) approach [5]. A custom mass transfer model for the phase-change was developed, which improves numerical stability by relaxing the phase change over a small temperature range, rather than enforcing it at a single threshold temperature. In order to ensure a sharp phase boundary during solidification, a very small time step size of the order of 10^{-6} s is required, while the heat conduction takes places in time scales of seconds, which is computationally challenging. Due to the elevated Reynolds numbers of $\mathcal{O}(10^3)$, estimated based on the strut diameter, the flow is expected to exhibit developing turbulence; which is not explicitly modeled here.

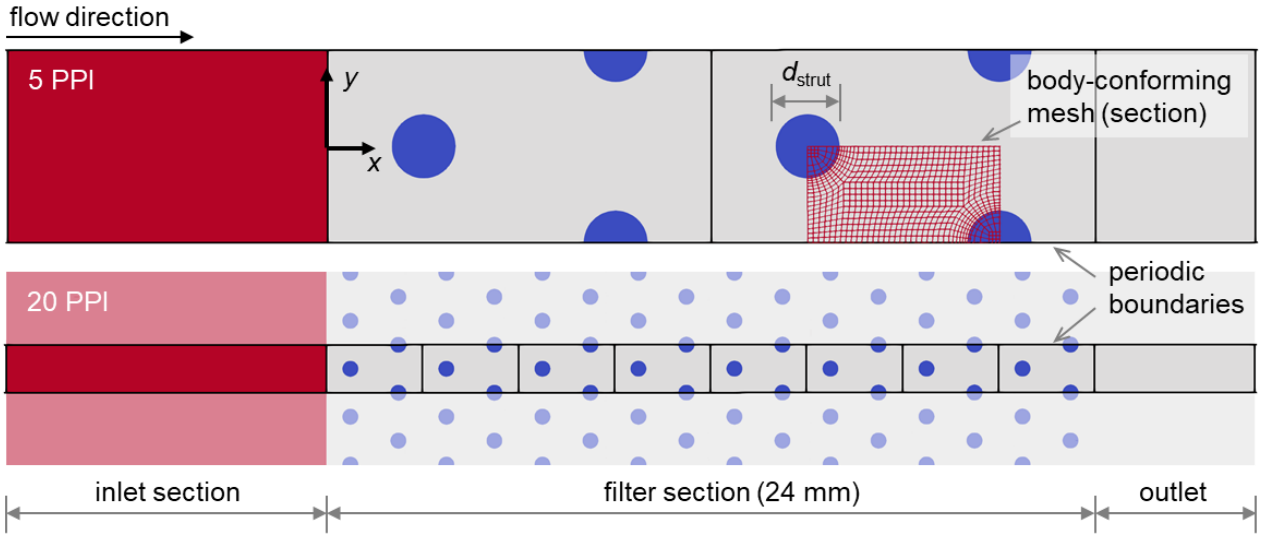

Figure 1 Sketch of the computational domain (outlined area) for pore counts of 5 and 20 PPI. The red area is initialized as liquid metal, the gray area as gas and the blue areas represent the filter struts

The validation of the numerical model was carried out through comparison with known solutions for standard problems, specifically the Laplace pressure inside a droplet and the time evolution of the phase boundary for the one-dimensional one-phase Stefan problem. The energy balance of all phases was monitored and ascertained.

2.2 Geometry modeling

In order to reduce the computational effort and facilitate parametric geometry variations, the open-cell filter foam was modelled as a 2D array of staggered cylinders [6]. The array is composed of periodic unit cells, as shown in **Figure 1**, which are repeated in axial direction to match the thickness of a typical CFF and allow the use of periodic boundary conditions in spanwise direction. It may be noted that effects of the lateral boundaries as well as axial heat conduction inside the filter structure cannot be captured using this approach. Furthermore, one cannot maintain similarity to the 3D structure with respect to both, strut diameter and porosity. Here, we have opted to match the strut diameter of typical CFFs at the cost of an increased porosity. The detailed data are provided in **Table 1**.

Table 1 Geometry properties of the idealized foam structure. The pore count (PPI) was estimated by comparison with the average pore diameter of industrial CFFs

Pore count		**5 PPI**	**8 PPI**	**10 PPI**	**15 PPI**	**20 PPI**
Unit cells		2	3	4	6	8
Strut diameter	mm	2.00	1.33	1.00 (0.6 - 1.2)	0.66	0.50
Av. pore diameter	mm	9.00	6.00	4.50-	3.00	2.25
Porosity		91%	91%	91% (87% - 97%)	91%	91%

3. RESULTS

In the following, simulations of Aluminum infiltration with constant flow rate and gravity driven flow will be presented. The simulations were carried out using the thermophysical properties provided in **Table 2**. The following reference conditions were applied: 730 °C initial melt temperature, 20 °C initial foam temperature, 0.1 m/s inlet velocity, 10 PPI pore count. The gas temperature was initialized as the arithmetic mean of initial melt and foam temperature. At the outlet boundary of the domain, a total gauge pressure of 0 Pa was imposed.

Table 2 Thermophysical properties used in the simulations. In order to avoid numerical issues associated with the volume change during phase transition, density and specific heat of liquid Aluminum were also assumed for the solid state

Property		**Liquid metal (Al)** [7]	**Solid metal (Al)** [7]	**Filter (Al_2O_3)** [8]	**Air** [9]
Density	$\mathrm{kg\ m^{-3}}$	2,380	2,380	3,970	0.5
Viscosity	$\mathrm{Pa}\ s$	$1.01 \cdot 10^{-3}$	-	-	$3.39 \cdot 10^{-5}$
Specific heat	$\mathrm{kJ\ kg^{-1}\ K^{-1}}$	1,180	1,180	1,100	1,075
Heat conductivity	$\mathrm{W\ m^{-1}\ K^{-1}}$	93.6	220	10	$5.24 \cdot 10^{-2}$
Melting temperature	°C	660			
Enthalpy of fusion	$\mathrm{kJ\ kg^{-1}}$	397	-	-	-
Surface tension	$\mathrm{N\ m^{-1}}$	0.86	-	-	-

3.1 Constant flow rate

In order to study the effect of flow velocity, a constant flow rate was imposed. **Figure 2** shows the distributions of temperature, fraction of solid Aluminum and velocity magnitude for a constant flow velocity of 10 cm/s at reference conditions. Although the metal loses heat to the filter struts, its temperature does not drop significantly due to the release of the latent heat during solidification. The freezing occurs near the upstream and lateral faces of the filter struts and forces the flow to take a more tortuous path. Two phase change regions can be identified: a solidification region near the melt front and a re-melting zone, which lags behind by a few pores. Further, small gas bubbles are entrained behind the filter struts and have been observed to coalesce into larger bubbles over time.

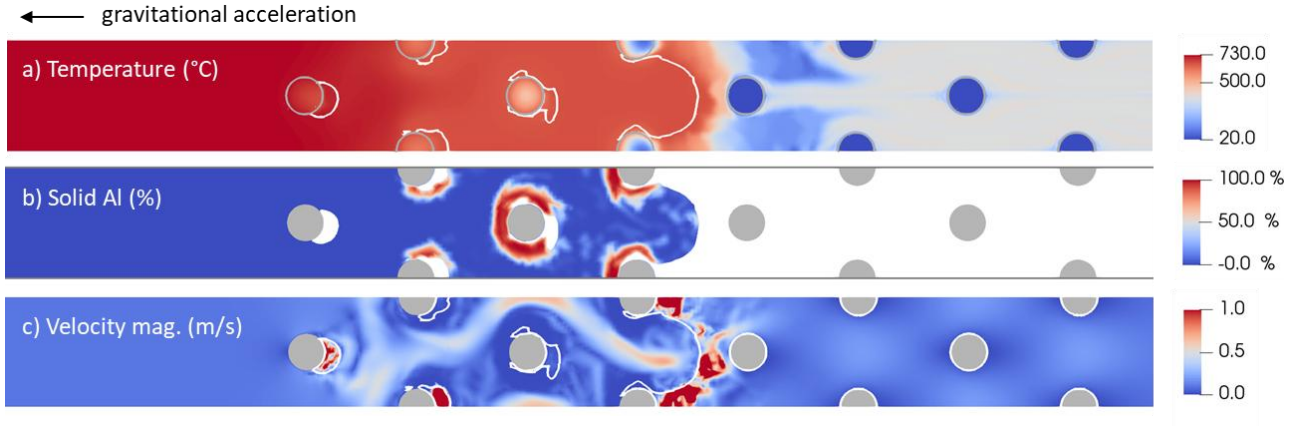

Figure 2 Distributions of a) temperature, b) Aluminum solid fraction and c) velocity magnitude for a superficial velocity of 0.1 m/s at time 0.1 s. The liquid/gas interface is indicated by the white line

Figure 3a depicts the variation of the average filter temperature over dimensionless time, obtained by normalization with the melt residence time inside the filter, which can be understood as a measure for the infiltration depth. While the temperature increases proportional to dimensionless time at low velocity, it follows with a delay at high velocity, i.e. a larger volume of melt contributes energy to the filter. As can be seen from **Figure 3b**, this leads to a smaller volume fraction of solidified metal. Nevertheless, as shown in **Figure 3c**, the pressure drop is very high due to the quadratic increase of inertial resistance with superficial velocity.

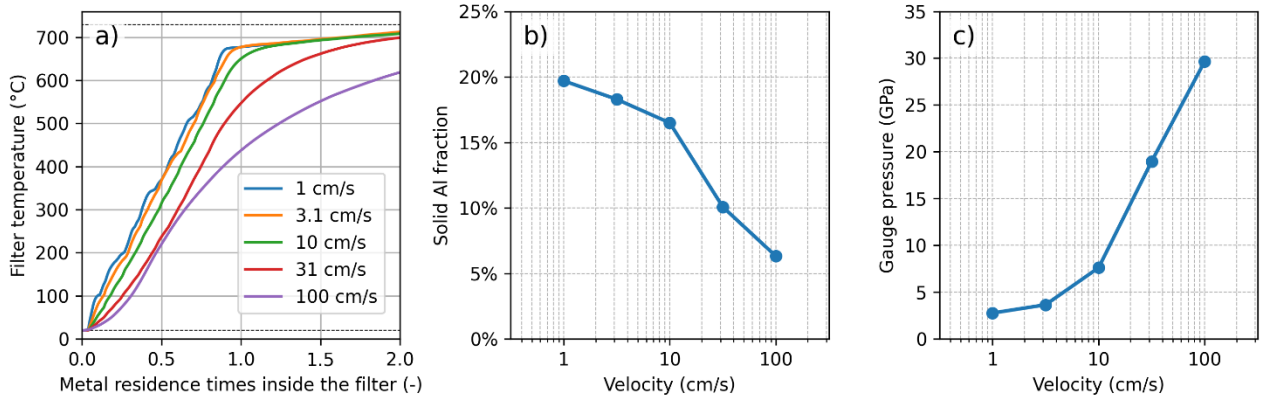

Figure 3 Variations of a) average filter temperature over dimensionless time (normalized with respect to average metal residence time inside the filter), b) solid fraction of Al and c) gauge pressure at the filter inlet for different flow velocity

The superficial velocity also influences the local distribution of solidification, shifting from the front to the sides of the filter struts with increasing velocity, which is not presented here for the sake of brevity.

As visible from **Figure 2c**, the numerical model generates unphysical spurious velocities, which are common for the CSF approach. Since they affect mainly the gas phase, their impact on the overall momentum and energy transport is believed to be small. A limitation of the enthalpy-porosity formulation becomes visible during the re-melting, when solidified portions seem to lose connection to the filter wall, but are still held in place as the resistance term attenuates the flow simply depending on the local solid fraction.

3.2 Gravity-driven flow

In order to model the infiltration conditions during top-poured gravity casting, the gravitational acceleration was aligned with the flow direction, the inlet section was extended to a length of 10 cm and at the inlet, an additional gauge pressure was imposed, representing the metallostatic head of a quiescent melt reservoir of 10 cm height. Under these conditions, the melt accelerates to a velocity of approx. 2 m/s before touching the filter.

Figure 4 shows the variation of melt velocity with time for different parameter variations. For almost all cases, the flow sharply decelerates within the first 0.1 s, as a consequence of primarily inertial resistance that is amplified by the flow constriction due to solidification. This is accompanied by a pressure increase at the filter inlet, of up to 59 kPa for the 20 PPI case. With progressing re-melting, the resistance decreases, causing the flow to accelerate and to eventually reach a terminal velocity. As expected, the deceleration and duration of slowdown increase with lower initial temperature of the foam, lower melt temperature, larger strut diameter and higher pore count. If the flow nearly stagnates, as is the case for pore counts of 15 and 20 PPI, the re-melting is significantly delayed, since the heat required to re-melt the solidified portions is mainly provided by axial conduction, which is much slower than the convective heat transfer. Gas bubbles, which were entrained by the turbulent melt front and coalesced, further aggravate this situation as they significantly reduce the effective thermal conductivity. In addition, the driving temperature difference is relatively low as the latent heat release during solidification prevents the temperature from falling significantly below the melting point. If the resulting axial heat flux is smaller than the heat losses to the surrounding, which are not taken into account here, the melt will freeze completely.

It should be noted that the terminal velocity of the flow through real CFFs would be lower, as the idealized geometry exhibits higher permeability due to its high porosity, regular structure, and the absence of small defects such as closed windows.

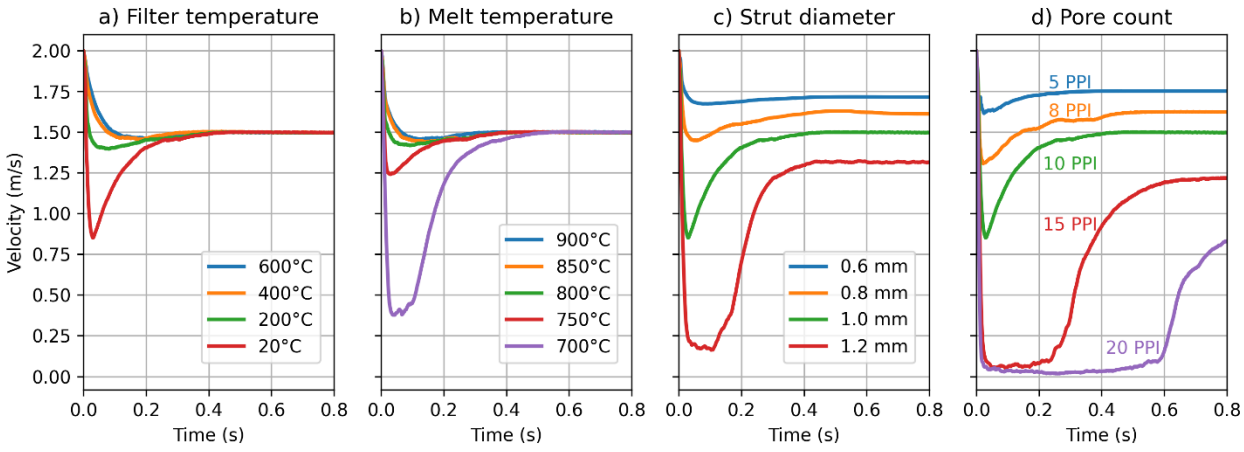

Figure 4 Time-series of flow velocity for different a) initial filter temperature, b) melt inlet temperature, c) strut diameter and d) pore count

4. CONCLUSIONS

This study presents a pore-scale numerical model for the simulation of liquid metal infiltration into CFFs under non-isothermal conditions. The model captures the key physical mechanisms governing the priming stage, including multiphase flow, heat transfer, phase change, and capillary effects. Its capability was demonstrated through a systematic parametric investigation of process conditions and geometric filter properties.

The results highlight the strong sensitivity of the infiltration process to pore density, porosity (strut diameter), melt superheat, initial filter temperature and flow conditions. In particular, higher pore densities, while beneficial for filtration efficiency during steady operation, significantly increase the risk of a temporary flow stagnation due to solidification. The findings are consistent with experimental observations and contribute to a more comprehensive understanding of the priming behavior of CFFs. In particular, entrained gas pockets were identified to substantially increase the risk of permanent freezing due to the reduction of effective thermal conductivity, impairing the heat transfer required for re-melting. Therefore, the filter design should also aim towards reducing the probability of incomplete infiltration or bubble entrainment through promoting a more uniform filling behavior.

Although the present simulation was carried out using an idealized two-dimensional geometry, the model is also applicable to real or artificial three-dimensional filter structures. The simulations can additionally provide input data for the detailed prediction of thermomechanical stresses and the mechanical failure behavior of the filter. Overall, the developed model provides a valuable tool for the design and optimization of ceramic foam filters, enabling a balanced consideration of priming behavior and filtration performance.

ACKNOWLEDGEMENTS

This work was funded by the Deutsche Forschungsgemeinschaft (DFG, German Research Foundation) - project ID 169148856 (transfer project T11).

REFERENCES

[1] OLSON III, R. A., MARTINS, L. C. B. Liquid Metal Filtration. In: *Cellular Ceramics - Structure, Manufacturing, Properties and Applications*. Weinheim: Wiley-VCH, 2005, pp. 403–415.

[2] WERZNER, E., MENDES, M. A. A., DEMUTH, C., TRIMIS, D., RAY, S. Simulation of Fluid Flow, Heat Transfer and Particle Transport Inside Open-Cell Foam Filters for Metal Melt Filtration. In: *Multifunctional Ceramic Filter Systems for Metal Melt Filtration: Towards Zero-Defect Materials*. Cham: Springer International Publishing, 2024, pp. 301–333.

[3] DESHPANDE, S. S., ANUMOLU, L., TRUJILLO, M. F. Evaluating the performance of the two-phase flow solver interFoam. *Computational Science & Discovery*. 2012, vol. 5, no. 1, 014016.

[4] PRAKASH, C., SAMONDS, M., SINGHAL, A. K. A fixed grid numerical methodology for phase change problems involving a moving heat source. *International Journal of Heat and Mass Transfer*. 1987, vol. 30, no. 12, pp. 2690–2694.

[5] BRACKBILL, J.U., KOTHE, D.B., ZEMACH, C. A continuum method for modeling surface tension. *Journal of Computational Physics*. 1992, vol. 100, no. 2, pp. 335–354.

[6] KUWAHARA, F., YAMANE, T., NAKAYAMA, A. Large eddy simulation of turbulent flow in porous media. *International Communications in Heat and Mass Transfer*. 2006, vol. 33, no. 4, pp. 411–418.

[7] MILLS, Kenneth C. *Recommended values of thermophysical properties for selected commercial alloys*. Cambridge: Woodhead Publishing, 2002.

[8] SHACKELFORD, J. F., ALEXANDER, W. (eds.). *CRC Materials Science and Engineering Handbook*. Boca Raton: CRC Press, 2000.

[9] INCROPERA, F. P., DEWITT, D. P., BERGMAN, T. L., LAVINE, A. S. *Fundamentals of Heat and Mass Transfer*. Hoboken, NJ: John Wiley & Sons, Inc., 2007.